IEEE Access
Multidisciplinary | Rapid Review | Open Access Journal

Received November 8, 2018, accepted April 23, 2019, date of publication April 30, 2019, date of current version May 14, 2019.

Digital Object Identifier 10.1109/ACCESS.2019.2913867

Detent Force Reduction in Permanent Magnet Linear Synchronous Motor Base on Magnetic Field Similarity Method

CHUNYUAN LIU[1], HUIMIN GAO[1], YUANSHENG XIONG[1], SHIGUI ZHOU[2], AND WENZHEN FU[1]
[1]College of Mechanical and Electrical Engineering, Jiaxing University, Jiaxing 314000, China
[2]School of Engineering, Qufu Normal University, Rizhao 276826, China

Corresponding author: Chunyuan Liu (liuchunyuan_zjx@163.com)

This work was supported in part by the Zhejiang Provincial Natural Science Foundation of China under Grant LY19E070004 and Grant 2016C31083, in part by the Natural Science Foundation of Shandong Province under Grant ZR2014EEM013, and in part by the Project of Jiaxing Science and Technology Bureau China under Grant 2017AY13017.

ABSTRACT Permanent-magnet linear synchronous motors (PMLSMs) have been widely used in various industries. However, the inherent detent force of these motors limits their application range, especially in high-precision motion and low-speed systems. In this study, magnetic field similarity (MFS) method and edgy teeth-shape optimization are proposed to reduce the detent force. First, an equivalent model of the PMLSM is established wherein the end effect is initially taken into consideration, and the parameters, such as reluctance, energy, and detent force, are calculated. Second, the principle of the MFS is introduced, and the main parameters that affect the detent force are obtained. The detent force is studied and analyzed using parametric analysis, and the shape of the edgy teeth is optimized by particle swarm optimization. The simulation verifies the correctness and applicability of the proposed method. Finally, a prototype is fabricated and the experimental results verify the validity of the mathematical model and simulation results.

INDEX TERMS Magnetic field similarity, equivalent magnetic circuit, finite element analysis, tubular permanent magnet linear generator, particle swarm optimization.

I. INTRODUCTION

Compared with traditional rotary drive systems, direct-drive (D-D) systems remove mechanical conversion components, which have higher efficiency, higher accuracy, and are maintenance-free. In the last few years, D-D systems have been widely used in industrial applications, such as numerically controlled machine tools [1]–[3], compressors [4], [5], and wave power take-off systems [6], [7]. Among the many kinds of topologies for linear motors, the permanent magnet linear synchronous motor (PMLSM) has the advantages of high force density, rapid dynamic response, and low thermal losses [8], [9]. Therefore, it is ideally suited to electrical power generating systems and other industrial applications. In recent years, the PMLSM has attracted the interest of many experts and scholars and has achieved research results [10]–[13]. However, the inherent detent force limits its applications. Detent force may cause system oscillations or even destroy the stability of the system, especially in high-precision motion and low-speed systems. Thus, reducing the detent force is a key technique and an important research field in PMLSM design.

The detent force consists of two parts [14], namely, cogging and end effect force. Cogging force is caused by the attraction between permanent magnets (PMs) and ferromagnetic cores, and end effect force is caused by the finite length of the stator core. Presently, various methods are being used to reduce detent force. PM pole pitch [15], [16] and skewed PM [17] technologies are used to reduce cogging force. However, such methods increase the processing difficulties and manufacturing costs of motors. End effect force is often reduced by choosing a suitable stator length[18], [19], or adds auxiliary slots [20].

A magnetic field similarity (MFS) method is proposed in this study to reduce the detent force of PMLSMs. The structure of this thesis is as follows. In Section II, an equivalent magnetic circuit model is established and the expression of the detent force is derived according to the principle of virtual work. In Section III, the optimization methods

The associate editor coordinating the review of this manuscript and approving it for publication was Bora Onat.

are proposed. In Section IV, a prototype is manufactured by the optimum results and the experiment results are discussed. Finally, the paper is summarized, and the current unsolved problem and direction for future research are presented.

II. STRUCTURE AND EQUIVALENT MAGNETIC CIRCUIT MODEL

The 3-D diagram structure of the designed PMLSM is illustrated in Fig. 1. The motor is composed of two parts: primary and secondary. The primary consists of the stator and the three-phase windings, and the secondary consists of the PMs and the back iron. Halbach magnetized PMs are employed because of the inherently sinusoidal waveform in the air gap field distribution and because they create an essentially sinusoidal electro-motive force waveform and simplify the power post-processing. A modular winding is employed, which offers significant advantages over conventional tubular machines. Each phase winding consists of concentrated coils that are disposed adjacent to each other, resulting in a high winding factor and a small number of slots for a given number of poles. Modular windings lower manufacturing costs and result in a fractional number of slots per pole. Thus, the cogging force caused by the stator slots can be very minimal [21], [22]. The main parameters of the PMLSM are shown in Table 1.

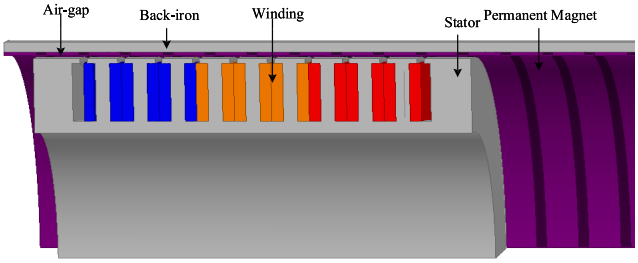

FIGURE 1. Structure of the PMLSM.

TABLE 1. Main parameters of the PMLSM.

Parameters	Items	Values
τ_s	Pole pitch	33.8 mm
τ_c	Slot pitch	30 mm
R_o	Outer radius	245 mm
R_i	Inner radius	150 mm
g	Air gap	3 mm
W_{te}	Width of end teeth	13 mm
H_y	Thickness of yoke	12 mm
W_s	Width of slot	18.6 mm
H_b	Thickness of back iron	10 mm
H_{pm}	Thickness of PM	3 mm
L_{pri}	Length of primary	311.4 mm

The reluctance of the PM, air gap, teeth, and yoke is considered. Leakage reluctance of the end teeth is also considered because of the edge effect. The primary iron and the back iron are assumed to be unsaturated because the flux density in the back iron is lower and the reluctance of the back iron is also neglected. The equivalent magnetic circuit (EMC) model is shown in Fig. 2.

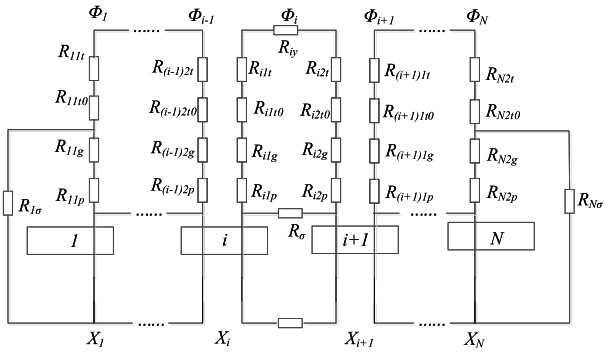

FIGURE 2. Equivalent mode of the PMLSM.

A general expression for the value of a reluctance is given as follows:

$$R_m = \frac{l_c H}{A_c B}, \tag{1}$$

where H is the magnetic field intensity in the circuit, B is the magnetic flux density in the circuit, l_c is the length of the magnetic circuit, and A_c is the cross section of the magnetic circuit.

With this equation, the air-gap reluctance R_g can be expressed as

$$R_g = \frac{K_c g}{\mu_0 \alpha_i l_{Fe}(b_t + b_s)}, \tag{2}$$

where K_c is the Carter factor, g is the length of the air gap, μ_0 is the magnetic permeability in the vacuum, α_i is the pole arc coefficient, l_{Fe} is the effective thickness of the laminated core, and b_t and b_s are the width of the teeth and the slot, respectively.

The reluctance of the PM is calculated as

$$R_p = \frac{h_{pm}/\mu_m}{\mu_0 \alpha_i l_{Fe} W_{pm}}, \tag{3}$$

where h_{pm} is the thickness of the PM, μ_m is the relative magnetic permeability of the PM, and W_{pm} is the width of the PM.

The expression of the teeth reluctance (R_t) and the yoke reluctance (R_y) are calculated respectively as

$$R_t = \frac{2h_t}{3b_t l_{Fe}}(150 + 15B_t^{10}) \tag{4}$$

and

$$R_y = \frac{b_y}{h_y l_{Fe}}(150 + 15B_t^{10}), \tag{5}$$

where h_t is the length of the teeth, B_t is the magnetic flux density of the teeth, b_y is the height of the yoke, and h_y is the translator yoke height.

The slot leakage reluctance R_σ is calculated as

$$R_\sigma = \frac{2b_s}{\mu_0 h_s l_{Fe}}, \tag{6}$$

where h_s is the slot height.

According to the magnetic circuit characteristics of the PMLSM, the *ith* magnetic flux ϕ_i is calculated in (7), as shown at the bottom of this page, where k_i is the coefficient of the flux distribution; F_{pm} is the magnetic motive force; h_{pm} is the thickness of the PM; H_c is the coercivity of the PM; and R_t, R_{t0}, R_g, R_{pm}, R_σ, and R_y are the reluctance of the teeth, teeth shoe, air gap, PM, leakage flux, and yoke, respectively.

The energy of the *ith* magnetic flux is calculated according to the formula of energy density $u_m = B^2/2\mu$. Therefore, the whole energy of the primary is

$$W = \sum_{i=1}^{N-1} [\frac{h_t+h_{t0}+h_{pm}+h_g}{2\mu_0 l_{Fe} W_{pm}} (\frac{\phi_i^2}{1-k_i} + \frac{\phi_i^2}{k_i+1}) + \frac{b_s \phi_i^2}{2\mu_0 l_{Fe} h_y}]. \tag{8}$$

Supposing that the relative position between the primary and secondary is x, the detent force can be calculated by the principle of virtual work as

$$\begin{aligned} F &= -\frac{\partial W}{\partial x} \\ &= -\sum_{i=1}^{N-1} [\frac{h_t + h_{t0} + h_{pm} + h_g}{2\mu_0 l_{Fe} W_{pm}} \frac{\partial}{\partial x} (\frac{\phi_i^2}{1-k_i} + \frac{\phi_i^2}{k_i+1}) \\ &\quad + \frac{b_s}{2\mu_0 l_{Fe} h_y} \frac{\partial \phi_i^2}{\partial x}]. \end{aligned} \tag{9}$$

III. DESIGN OPTIMIZATION AND COMPARATIVE STUDY

The design optimization of the PMLSM is a nonlinear constrained and mixed discrete multiple variable optimization problem. The material cost, output power, and minimum detent force are important issues in PMLSM design. The improvement of the output power is often accompanied by an increase in material costs. Therefore, it is impossible to achieve the optimum for each objective. The corresponding optimal solutions are a compromise between the objectives by making them as close to their optimums as possible. In this study, the goal of optimization is to obtain the minimum detent force and the maximum output power without increasing the material costs. As no core disconnection exists in the rotating motor and the longitudinal end effect does not exist, the magnetic circuit distribution of the rotating machine is completely symmetrical. However, the longitudinal end effect exists in the linear motor from the disconnection of both sides. The longitudinal end effect not only causes distortions in the air magnetic field on both sides but also affects the distribution of the magnetic field in the core. Therefore, to address the different magnetic fields between the rotary and the linear motor, the MFS method is proposed to reduce the detent force.

A. MFS METHOD

Compared with the linear and the rotary motor, the distribution of the magnetic field of each magnetic pole is equal in size to the loop magnetic flux formed by the two adjacent magnetic poles under the rotary motor. However, the distribution of the magnetic field in each pole is uneven under the linear motor. Therefore, the longitudinal end effect causes the unevenly distributed magnetic field in each magnetic circuit. If a reasonable method can be employed to equalize the distribution of the magnetic field in the linear motor and the rotary motor, the longitudinal end effect may be eliminated and the detent force may be effectively decreased.

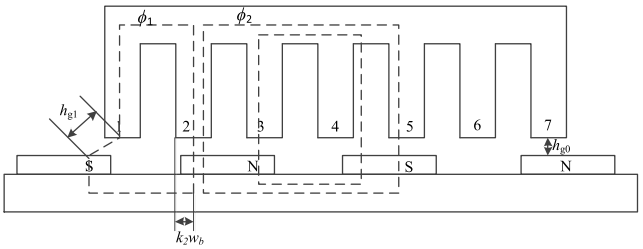

FIGURE 3. Magnetic field distribution of a PMLSM.

According to the principle of basic magnetic circuit, the magnetic field lines start from the N pole and close at the S pole. The dotted line describes the magnetic field distribution in the no-load condition, as shown in Fig.3. To analyze the magnetic field that crosses each tooth, the distribution coefficient of the magnetic circuit k_i expresses the proportion of the tooth width in the i-th tooth and the $(i-1)$th tooth, which forms the magnetic circuit for the i-th tooth to the entire tooth width with the value of 0–1. Its value depends on the magnetic resistance of the two parallel magnetic circuits. The magnetic circuit is not saturated when there is no current in the winding and the reluctance mainly comes from the air gap and the PM, which is approximately the ratio of the equivalent air gap to the thickness of the PM. The parameters are shown in Fig. 3. The k_2 is calculated as follows:

$$\frac{k_2 W_b}{(1-k_2) W_b} = \frac{R_{\phi 2}}{R_{\phi 1}} \approx \frac{h_{g0} + h_{PM}}{h_{g1} + h_{PM}}, \tag{10}$$

where W_b is the width of the teeth; $R_{\phi 1}$ and $R_{\phi 2}$ are the reluctance of $\phi 1$ and $\phi 2$, respectively; h_{g0} is the air gap; and h_{g1} is the equivalent air gap of the side teeth.

We assume that the distribution of the PMLSM is uniform and the coefficients of the flux distribution are all equal to k_1.

$$\begin{aligned} \phi_i &= \frac{2 \times F_{pm}}{R_{i1pm} + R_{i1g} + R_{i1t0} + R_{i1t} + R_{i2t} + R_{i2t0} + R_{i2g} + R_{i2pm} + R_y + R_\sigma} \\ &= \frac{2 \times H_c \times h_m}{(R_t + R_{t0} + R_g + R_{pm} + R_\sigma) \frac{k_i(1-k_i)}{k_i+(1-k_i)} + R_y} \end{aligned} \tag{7}$$

Therefore, the flux of the first magnetic circuit ϕ_{1L} is given in the following equation:

$$\phi_{1L} = \frac{2F}{R_{1L}} = k_1 \frac{2}{h_g + h'_g + 2h_{PM}}, \tag{11}$$

where h'_g is the equivalent air gap of the first teeth.

Compared with the rotary motor, the flux of the first magnetic circuit ϕ_{1R} is

$$\phi_{1R} = \frac{2F}{R_{1R}} = k_1 \frac{2}{2h_g + 2h_{PM}}. \tag{12}$$

Therefore, if $\phi_{1L} = \phi_{1R}$, then the end effect can be ignored in the linear motor and the air gap and the equivalent air gap of the first teeth is satisfied with

$$h_g = h'_g. \tag{13}$$

The equivalent air gap for the first magnetic circuit should be equal to the air gap for the rotary motor to have the same magnetic field distribution. Moreover, the slot topology of the rotary machine is the same as that of the PMLSM. Therefore, if the longitudinal end effect of the PMLSM is eliminated, then the magnetic field distribution for the PMLSM will be uniform as long as the first equivalent air gap is the same as the intermediate air gap. The longitudinal end effect is eliminated and the detent force is reduced. This method is called the MFS.

According to the aforementioned principle, two methods can be used to eliminate the longitudinal end effect. The first is to increase the width of the end teeth, and the second is to decrease the actual air gap of the end teeth. The latter methodology may reduce the power density. The distribution of the magnetic field for the end tooth with the (a) original structure and the (b) optimized structure are shown in Fig. 4. A part of the leakage magnetic flux in (a) becomes the main magnetic flux in (b). Thereby, the rate of change of the magnetic flux is decreased and the end force is effectively reduced.

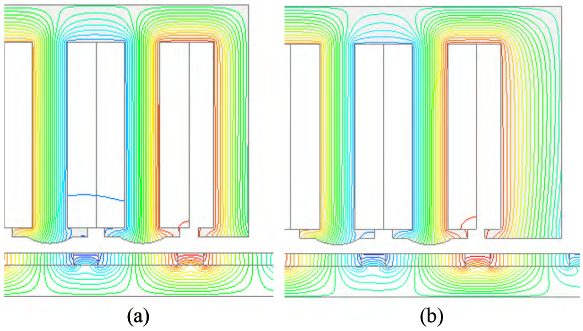

FIGURE 4. Distribution of magnetic field. (a) Original structure. (b) Optimized structure.

The detent force for the original and optimized end teeth structures are shown in Fig. 5, and the negative and positive maximum detent force for the original and optimized end teeth structures are shown in Table 4. The detent force

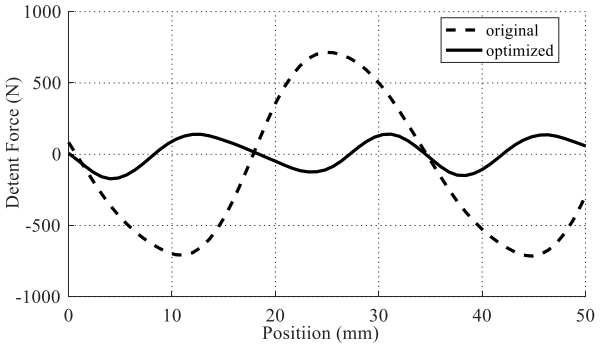

FIGURE 5. Detent force for different end teeth structures.

TABLE 2. Negative and positive peak detent force for different end teeth structures.

End teeth structure	Positive maximum value (*N*)	Negative maximum value (*N*)
original	714.9	719.3
optimized	141.0	172.3

is effectively reduced after optimization. Compared with the original structure, the positive and negative values are decreased 80.3% and 76.1%, respectively, after optimization.

B. OPTIMIZED PRIMARY LENGTH

The end effect force is caused by the disconnection of the PMLSM at both ends of the linear motor. According to Formula (9), the end effect is directly related to the length of the primary (L_{pri}) and can be decreased by optimizing the parameter of L_{pri}. To verify the accuracy of the analysis above, a 2-D finite element analysis (FEA) model is established according to the data of Table 1. Detent force is calculated using the parametric analysis for different lengths of the primary. The calculated results are shown in Fig. 6. The detent force is smallest when the length of the primary is equal to 326.7 mm. The negative and positive detent force maximum values for the different primary lengths are compared to further demonstrate the effectiveness of this method and are shown in Table 3. Compared to when L_{pri} equals 323.7 mm, when L_{pri} equals 326.7 mm, the positive and negative values are decreased by 64.2% and 64.3%, respectively. The FEA

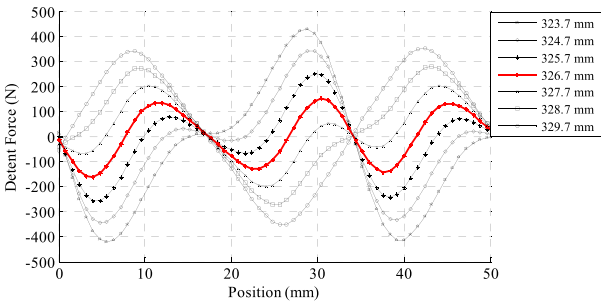

FIGURE 6. Detent force for different primary lengths.

TABLE 3. Comparison of the negative and positive maximum detent force values for different primary lengths.

Primary length (mm)	Positive maximum value (*N*)	Negative maximum value (*N*)
323.7	427.2	422.4
324.7	340.1	345.1
325.7	249.6	256.3
326.7	151.2	150.9
327.4	203.5	210.2
328.7	279.1	285.4
329.7	351.7	365.1

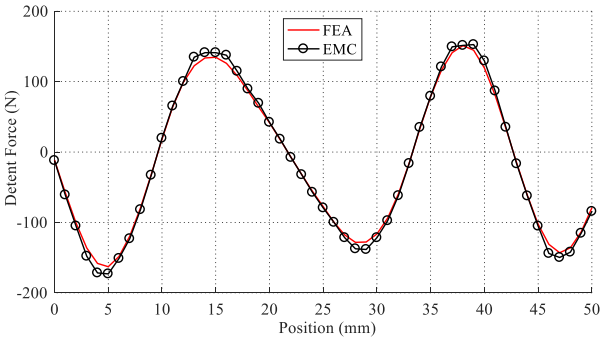

FIGURE 7. Comparison of FEA and EMC.

and the EMC are compared in Fig. 7, wherein the EMC solutions agree extremely well with the finite element results.

C. OPTIMIZED SHAPE OF AIR GAP AND EDGE TEETH

The electromagnetic energy conversion of the motor mainly occurs in the air gap. Therefore, a strong relationship exists between the structure and length of the air gap area and the electromagnetic performance, including the detent force. The detent force caused by the longitudinal end effect is optimized through the shape of the edge teeth and the air gap. The parameters are defined in Fig. 8. The design object is defined as the minimum detent force in its peak-to-peak value. The particle swarm optimization (PSO) algorithm is employed in this study, and the flowchart for the PSO algorithm is shown in Fig. 9. Detailed descriptions of the PSO algorithm can

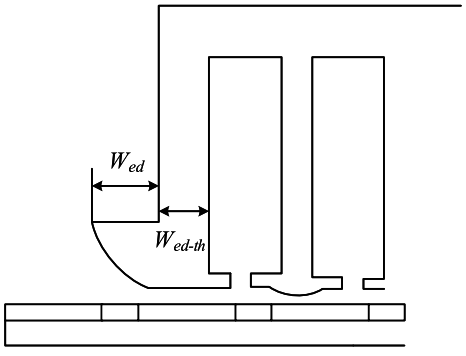

FIGURE 8. Design parameters for the edge teeth and the air gap.

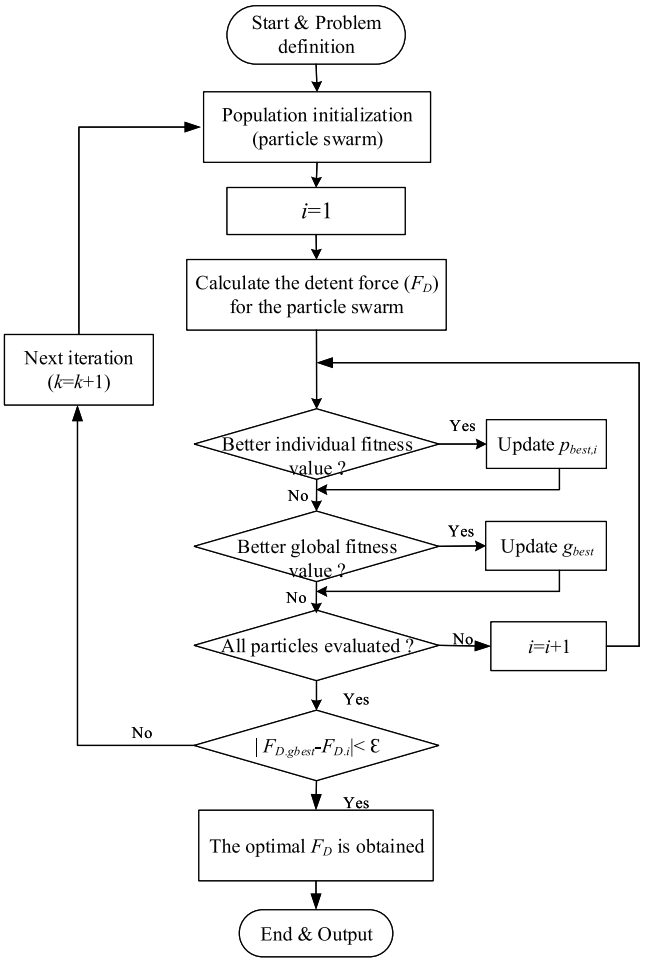

FIGURE 9. Flowchart for the PSO method.

be found in Ref. 23 and 24. The parameters W_{ed_th} (width of the edge teeth) and W_{ed} (width of the bulge edge teeth) are optimized by the PSO algorithm. The specific parameters after optimization are shown in Table 4.

TABLE 4. Optimized parameters.

Parameter	Items	Value
L_{pri}	Length of primary	326.7 mm
W_{ed}	Width of bulge tooth	18 mm
W_{ed_th}	Width of edge tooth	14.4 mm

The detent force for the traditional and arc structures are shown in Fig. 10. The negative and positive maximum detent force of the two types of air gap structures are shown in Table 5. The detent force in the air gap arc structure is smaller than that in the traditional structure.

According to the principle of virtual work, cogging forces can be expressed as follows:

$$F = -\frac{\partial W}{\partial x} = -\frac{1}{2}\varphi_g^2 \frac{\partial R_g}{\partial x}, \tag{14}$$

where φ_g is the air gap flux. The distribution of the magnetic field in the (a) traditional and (b) optimized arc structures are

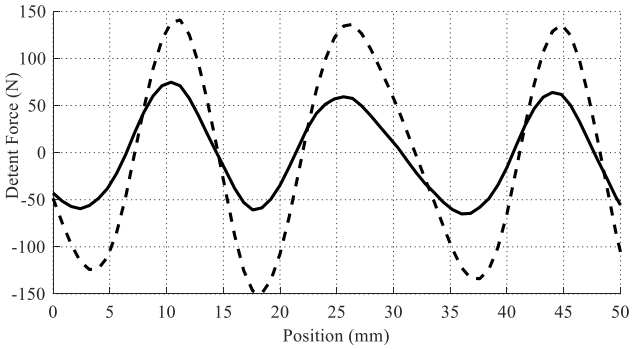

FIGURE 10. Detent force for original and optimized structures.

TABLE 5. Negative and positive maximum detent force values for different air gap structures.

Air gap structure	Positive maximum value (N)	Negative peak maximum (N)
Traditional	141.0	172.3
optimized arc	64.0	65.0

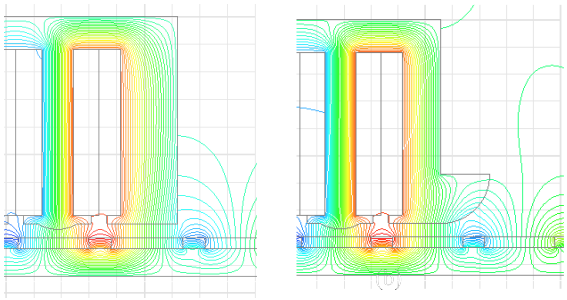

FIGURE 11. Distribution of magnetic field. (a) Traditional structure. (b) Optimized arc structure.

shown in Fig. 11. The effective air gap volume is increased for the optimized arc structure, which results in a decrease of the flux rate, in turn causing the reduction of the position rate of change for the magnetic field energy and reducing the cogging force. A comparison of the negative and positive detent force maximum values for different air gap structures are shown in Table 4. Compared with the traditional structure, the positive and negative detent force values for the optimized arc structure are decreased by 54.6% and 62.3%, respectively.

IV. EXPERIMENTAL TEST RESULTS

To verify the validity of the optimization methods and the simulation results, a prototype was fabricated as shown in Fig. 11. The secondary and the primary are shown in Fig. 12. The parameters of the prototype are designed according to the optimization results. The designed generator is used to convert wave energy into electric energy. Therefore, the structure of the outer secondary is employed to conveniently install the buoy and increase the power density. Through the investigation discovery, the wave height is

FIGURE 12. Prototype.

approximately 0.7–1.5 m, and the wave length is approximately 10–30 m in the experimental sites. Thus, a stroke length of 1.6 m is chosen.

The detent force measurement mainly adopts the method called the direct measurement of two-way reciprocating motion. The basic principle of this method states that the frictional force is the same as the magnitude, but they go in different directions in the same location. The detent force can be accurately measured because this method can counteract the influence of the frictional force. The PM linear motor has a reciprocating motion under a low-speed condition, in which the pull force is simultaneously measured by a force sensor. The principle diagram for the detent force measurement system is shown in Fig. 13. When the PMLSM is moving upward at low speed, the force equation is as follows:

$$F_U(x) - f(x) - F_{\mathrm{d}}(x) = Mg. \tag{15}$$

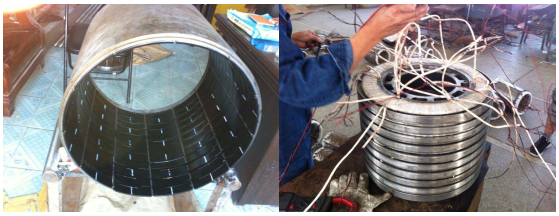

FIGURE 13. Secondary and primary. (a) Secondary. (b) Primary.

When the motor is moving downward at low speed, the force equation is as follows:

$$F_{\mathrm{D}}(x) - F_d(x) = Mg - f(x), \tag{16}$$

where $F_U(x)$ and $F_D(x)$ are the upward and downward forces for the measurement values of the sensor, respectively; $F_d(x)$ is the detent force; $f(x)$ is the friction; M is the mass of primary of the motor; and x is the relative location between the primary and the secondary.

According to Formulas (15) and (16), the expression for the detent force of is obtained as

$$F_d(x) = \frac{F_{\mathrm{D}}(x) + F_U(x) - 2Mg}{2}. \tag{17}$$

The test process is shown in Fig. 14. The measurement is performed three times on each point, and the average data are taken as the detent force. The data for the measurement and the FEA are shown in Fig. 15. The trend of the detent force

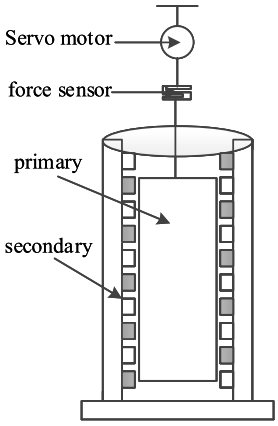

FIGURE 14. Principle diagram for detent force measurement.

FIGURE 15. Measurement of detent force.

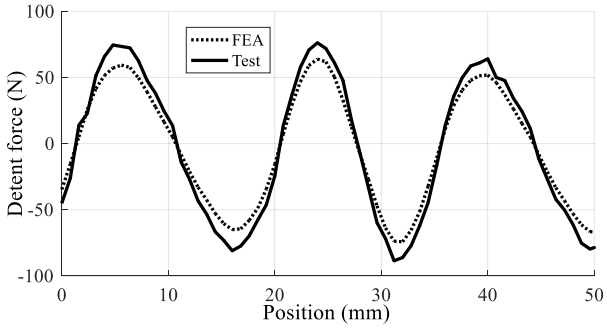

FIGURE 16. Comparison values for the measurement and the FEA.

has good agreement with the FEA, and the experiment shows the validity of the aforementioned method. However, the data for the measurement are larger than the FEA. The main reason for the difference between the experiment and the FEA is that some factors were ignored during the numerical calculation, such as the eddy current and stray losses, because the experiment system was working at a low-speed condition. Therefore, the frequency of the generator is considerably lower than the power frequency.

V. CONCLUSIONS

This study presented the methods to reduce detent force and end effect force by optimizing the length and shapes of the sides of the primary. In addition, the cogging force was reduced by optimizing the primary slots and the air gap structure according the principle of the MFS method. The equivalent magnetic circuit model was established considering the end effect. According to the energy density, the expression of the detent force was calculated using the parameters K_i, l_{Fe}, and so on. Through the calculations, the following conclusions are presented:

1) A strong relationship exists between the detent force and the length of the primary, and optimizing the length of the primary can greatly reduce the detent force. To analyze the proposed model, the positive and the negative detent force values may be reduced by 64.2% and 64.3%, respectively.

2) The shape of air gap influences the detent force. The distribution of the magnetic field changes when the shape of air gap changes, reducing the position rate of change for the magnetic field energy. Therefore, the detent force is greatly reduced.

3) The detent force may be effectively reduced by optimizing the shape of the end teeth. Compared with the original shape, the positive and negative values are decreased by 50.6% and 50.7%, respectively, after optimization.

REFERENCES

[1] S.-U. Chung and J.-M. Kim, "Double-sided iron-core PMLSM mover teeth arrangement design for reduction of detent force and speed ripple," *IEEE Trans. Ind. Electron.*, vol. 63, no. 5, pp. 3000–3008, May 2016.

[2] N. Xi and J.-J. Yang, "Optimal design of short-armature slotted type multi-segment permanent magnet linear synchronous motor for numerically controlled machine tool," *Int. J. Appl. Electromagn. Mech.*, vol. 47, no. 1, pp. 273–282, 2015.

[3] M. Soshi, F. Rigolone, J. Sheffield, and K. Yamazaki, "Development of a directly-driven thread whirling unit with advanced tool materials for mass-production of implantable medical parts," *CIRP Ann.*, vol. 67, no. 1, pp. 117–120, 2018.

[4] A. Hassan, A. Bijanzad, and I. Lazoglu, "Dynamic analysis of a novel moving magnet linear actuator," *IEEE Trans. Ind. Electron.*, vol. 64, no. 5, pp. 3758–3766, May 2017.

[5] M. Park, J. Lee, H. Kim, and Y. Ahn, "Experimental and numerical study of heat transfer characteristics using the heat balance in a linear compressor," *Int. J. Refrig.*, vol. 74, pp. 550–559, Feb. 2017.

[6] L. Huang, M. Hu, H. Yu, C. Liu, and Z. Chen, "Design and experiment of a direct-drive wave energy converter using outer-PM linear tubular generator," *IET Renew. Power Gener.*, vol. 11, no. 3, pp. 353–360, Feb. 2017.

[7] C. Liu, H. Yu, M. Hu, Q. Liu, S. Zhou, and L. Huang, "Research on a permanent magnet tubular linear generator for direct drive wave energy conversion," *IET Renew. Power Gener.*, vol. 8, no. 3, pp. 281–288, Apr. 2014.

[8] K.-B. Jang, J.-H. Kim, H.-J. An, and G.-T. Kim, "Optimal design of auxiliary teeth to minimize unbalanced phase due to end effect of PMLSM," *IEEE Trans. Magn.*, vol. 47, no. 5, pp. 1010–1013, May 2011.

[9] C.-C. Hwang, P.-L. Li, and C.-T. Liu, "Optimal design of a permanent magnet linear synchronous motor with low cogging force," *IEEE Trans. Magn.*, vol. 48, no. 2, pp. 1039–1042, Feb. 2012.

[10] B. Li, J. Zhao, X. Liu, Y. Guo, H. Hu, and J. Li, "Detent force reduction of an arc-linear permanent-magnet synchronous motor by using compensation windings," *IEEE Trans. Ind. Electron.*, vol. 64, no. 4, pp. 3001–3011, Apr. 2017.

[11] X. Liu, J. Gao, S. Huang, and K. Lu, "Magnetic field and thrust analysis of the U-channel air-core permanent magnet linear synchronous motor," *IEEE Trans. Magn.*, vol. 53, no. 6, Jun. 2017, Art. no. 8201504.

[12] K.-H. Shin, H.-I. Park, K.-H. Kim, S.-M. Jang, and J.-Y. Choi, "Magnet pole shape design for reduction of thrust ripple of slotless permanent magnet linear synchronous motor with arc-shaped magnets considering end-effect based on analytical method," *AIP Adv.*, vol. 7, no. 5, 2017, Art. no. 056656.
[13] Z. Zhang, H. Zhou, J. Duan, and B. Kou, "Design and analysis of a new ring winding structure for permanent magnet linear synchronous motors," *IEEE Trans. Plasma Sci.*, vol. 44, no. 12, pp. 3311–3321, Dec. 2016.
[14] M. Wang, L. Li, and D. Pan, "Detent force compensation for PMLSM systems based on structural design and control method combination," *IEEE Trans. Ind. Electron.*, vol. 62, no. 11, pp. 6845–6854, Nov. 2015.
[15] X. Z. Huang, J. Li, Q. Tan, C. M. Zhang, and L. Li, "Design principles of a phase-shift modular slotless tubular permanent magnet linear synchronous motor with three sectional primaries and analysis of its detent force," *IEEE Trans. Ind. Electron.*, vol. 65, no. 12, pp. 9346–9355, Dec. 2018.
[16] L. J. Wu, Z. Q. Zhu, D. A. Staton, M. Popescu, and D. Hawkins, "Comparison of analytical models of cogging torque in surface-mounted PM machines," *IEEE Trans. Ind. Electron.*, vol. 59, no. 6, pp. 2414–2425, Jun. 2012.
[17] H. Hu, X. Liu, J. Zhao, and Y. Guo, "Analysis and minimization of detent end force in linear permanent magnet synchronous machines," *IEEE Trans. Ind. Electron.*, vol. 65, no. 3, pp. 2475–2486, Mar. 2018.
[18] B. L. J. Gysen, K. J. Meessen, J. J. H. Paulides, and E. A. Lomonova, "3-D analytical and numerical modeling of tubular actuators with skewed permanent magnets," *IEEE Trans. Magn.*, vol. 47, no. 9, pp. 2200–2212, Sep. 2011.
[19] C. Liu, H. Yu, M. Hu, Q. Liu, and S. Zhou, "Detent force reduction in permanent magnet tubular linear generator for direct-driver wave energy conversion," *IEEE Trans. Magn.*, vol. 49, no. 5, pp. 1913–1916, May 2013.
[20] S.-W. Seo, G.-H. Jang, M.-M. Koo, and J.-Y. Choi, "Characteristic analysis of the influence of auxiliary teeth and notching on the reduction of the detent force of a permanent magnet linear synchronous machine," *IEEE Trans. Appl. Supercond.*, vol. 28, no. 3, Apr. 2018, Art. no. 5203705.
[21] C. F. Wang, J. X. Shen, Y. Wang, L. L. Wang, and M. J. Jin, "A new method for reduction of detent force in permanent magnet flux-switching linear motors," *IEEE Trans. Magn.*, vol. 45, no. 6, pp. 2843–2846, Jun. 2009.
[22] J. Wang and D. Howe, "Tubular modular permanent-magnet machines equipped with quasi-Halbach magnetized magnets—Part I: Magnetic field distribution, EMF, and thrust force," *IEEE Trans. Magn.*, vol. 41, no. 9, pp. 2470–2478, Sep. 2005.
[23] K. L. Lian, J. H. Jhang, and I. S. Tian, "A maximum power point tracking method based on perturb-and-observe combined with particle swarm optimization," *IEEE J. Photovolt.*, vol. 4, no. 2, pp. 626–633, Mar. 2014.
[24] Z. Xue, H. Li, Y. Zhou, N. Ren, and W. Wen, "Analytical prediction and optimization of cogging torque in surface-mounted permanent magnet machines with modified particle swarm optimization," *IEEE Trans. Ind. Electron.*, vol. 64, no. 12, pp. 9795–9805, Dec. 2017.

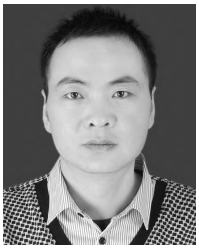

CHUNYUAN LIU received the Ph.D. degree from Southeast University, Nanjing, China, in 2015. He has been a Teacher with the College of Mechanical and Electrical Engineering, Jiaxing University, China. His current research interests include the design, analysis, and control of electrical machines, and conversion and utilization of new energy.

HUIMIN GAO received the Ph.D. degree from Xi'an Jiaotong University, Xi'an, China, in 2003. From 2009 to 2010, he was a Visiting Scholar with the University of Illinois at Urbana–Champaign, hosted by Prof. D. E. Goldberg. He is currently a Professor and the Deputy Dean of the School of Mechanical and Electrical Engineering, Jiaxing University, Jiaxing, China. He has published more than 40 papers. His research interests include the modeling, simulation and scheduling of complex systems. He is currently the Editorial Board Member of the *Journal of System Simulation*.

YUANSHENG XIONG received the M.S. and Ph.D. degrees in control science and engineering from the Zhejiang University of Technology, Hangzhou, China, in 2004 and 2010, respectively. Since 2012, he has been an Assistant Professor with the College of Mechanical and Electrical Engineering, Jiaxing University, Jiaxing, China. His research interests include the power generation and control of new energy, motion control, and embedded systems.

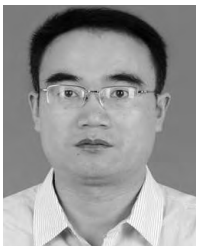

SHIGUI ZHOU received the Ph.D. degree from Southeast University, Nanjing, China, in 2013. He has been with Qufu Normal University, where he is currently an Associate Professor with the School of Engineering. His current research interest includes the design, analysis, and control of electrical machines.

WENZHEN FU received the M.S. degree in electrical engineering and automation from the South China University of Technology, in 2009. Her research interests include wireless energy transmission, designed and implemented of switching power supply, and the application of micro inverter in photovoltaic systems.